a

Thermocouples (6)   Aperture for collimator

Blackbody Cavity

Radiation shields (5)

Guard heater

Radiation shields (5)

Dia. ~25 cm

b

10 cm

Blackbody & Guard
(hand-wound heaters)

c

Radiation Shields (polished copper; 15 total)

Supplementary Figure 1 | Design of Blackbody Cavity (BBC). **a**, Guarding + shielding concept (CAD drawing) ensures 99% of the BBC's heater power transmits through the aperture instead of leaking out through the BBC side walls or supports. **b**, Home-built BBC and guard with hand-wound heaters ensure good temperature stability and uniformity ($T_{max} - T_{min} < 1.5$ K, as measured by six K-type thermocouples as shown in **a**). **c**, 15 radiation shields made of polished copper: five concentric "cans" for the BBC (middle row), five for the guard (back row), and five for the pyramidal test section (front row, assembled).
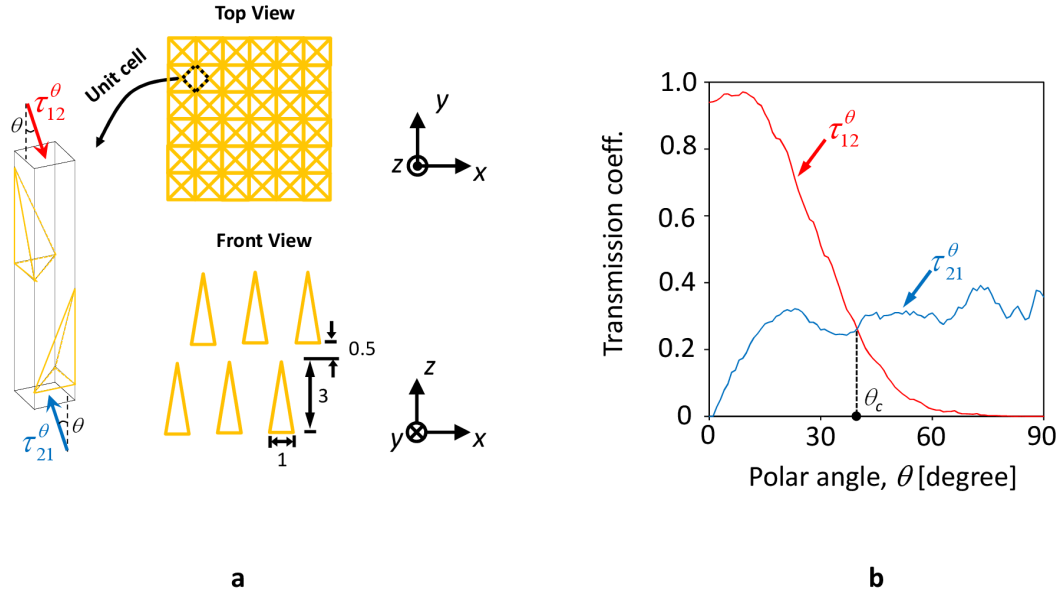
Supplementary Figure 2 | Ray tracing simulation to optimize the transmission function. a, Simulation domain: staggered double-layer pyramidal arrays (each layer a checkerboard) with specular surfaces and high aspect ratio for each pyramid. Mirror symmetries are applied to reduce the simulation domain to the unit cell indicated by the black dashed square. **b**, Simulation results for the geometry indicated in (a) and used in the main experiments. For photons launched from the top (τ_{12}^{θ}, red line), as incident angle increases, transmission decreases from ~95% to 0%. On the other hand, for photons launched from the bottom (τ_{21}^{θ}, blue line), as incident angle increase, transmission increases from 0% to ~35%.

a, View towards points (τ_{12}^{θ})

**b,** View towards bases (τ_{21}^{θ})
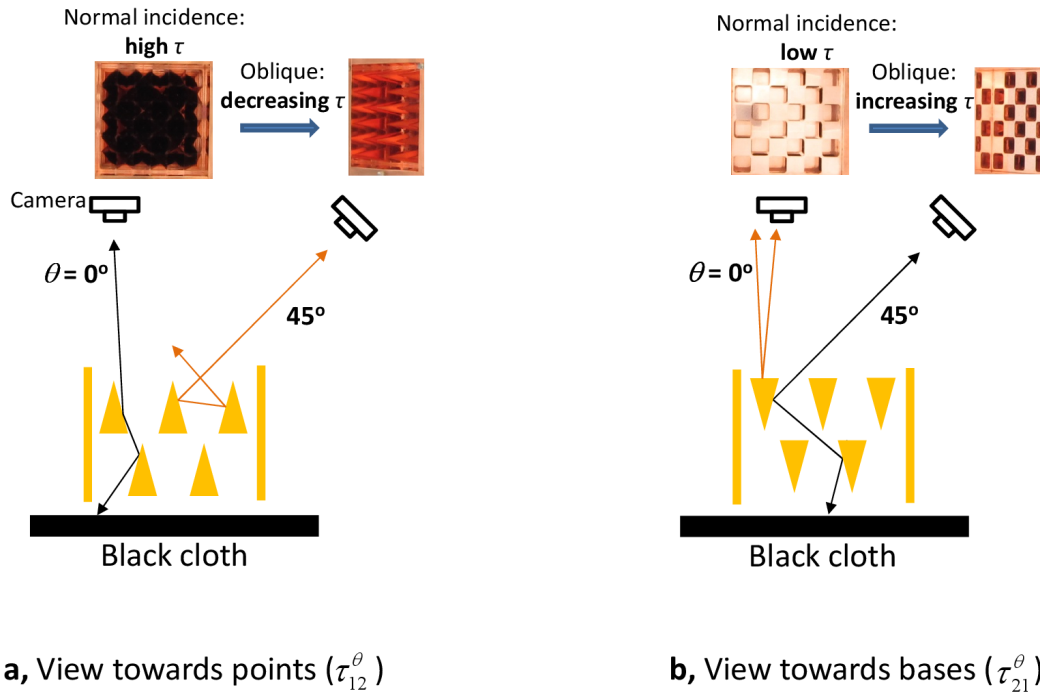
Supplementary Figure 3 | Visualization to confirm the function of the pyramidal test section. The surrounding environment is white (not shown), and the camera exposure time is the same for all images. **a,** View towards points. Mostly black from $\theta = 0^{\circ}$, indicating high transmission, while much less black from $\theta = 45^{\circ}$, indicating lower transmission. **b,** View towards bases. Mostly shiny from $\theta = 0^{\circ}$, indicating low transmission, while much more black from $\theta = 45^{\circ}$, indicating higher transmission.
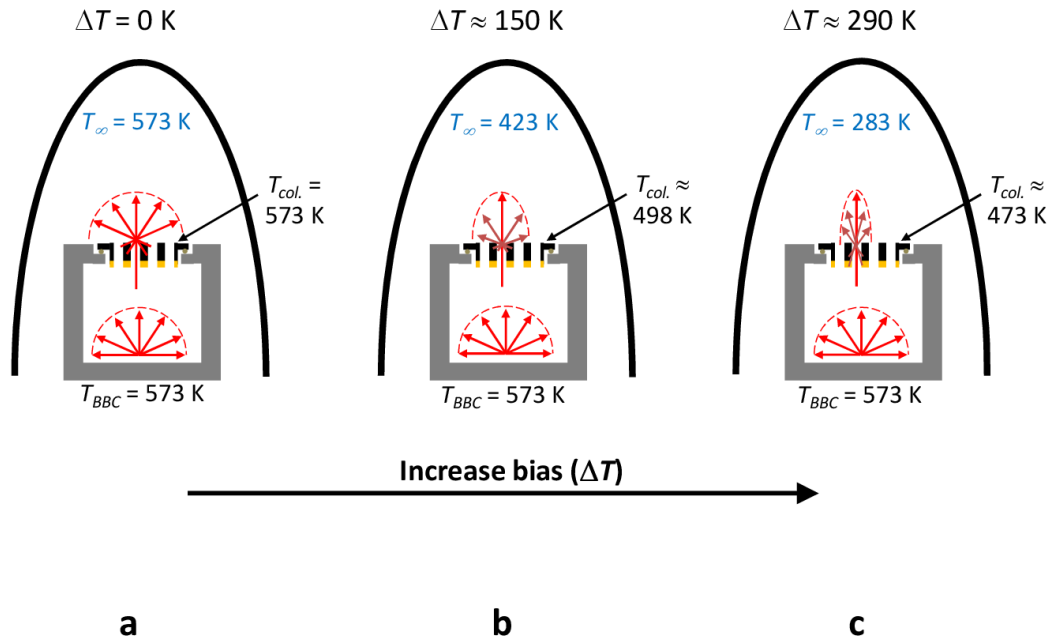
Supplementary Figure 4 | Conceptual evolution of the weighting function, $w(\theta)$. a, Zero bias ($\Delta T = 0$ K): the whole system is in equilibrium at 573 K, so that w does not depend on θ. **b**, Moderate bias ($\Delta T = 150$ K): the temperature of collimator, $T_{col.}$, is lower than that of BBC, T_{BBC}, so that w is somewhat distorted. **c**, large bias ($\Delta T = 290$ K; this corresponds to the main experiments): $T_{col.}$ is further reduced relative to T_{BBC}, so that w is further distorted. For an approximate analysis of this concept, see Supplementary Figs. 6-8.
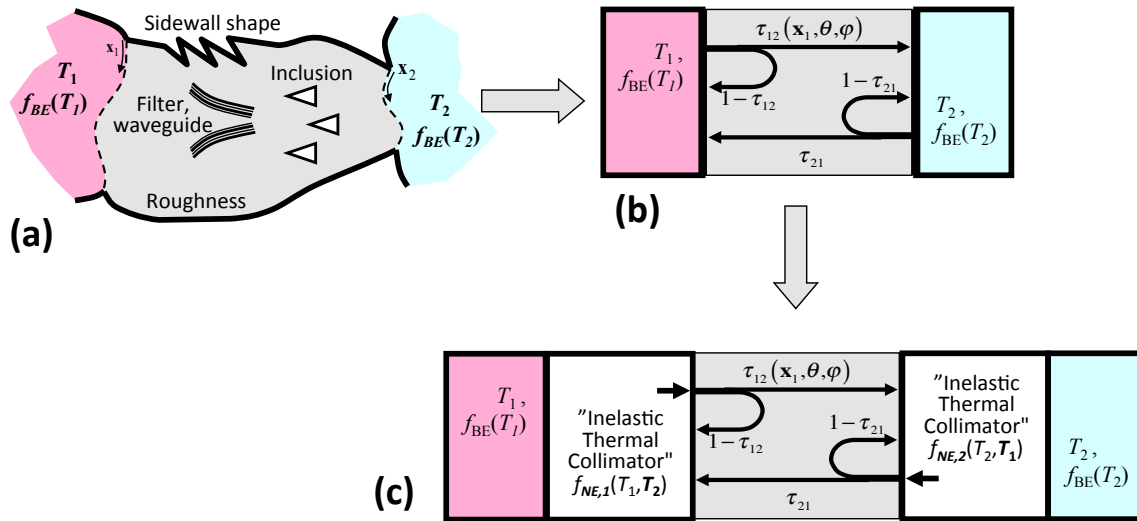
Supplementary Figure 5 | Landauer-Büttiker approach for modeling heat transfer in a two-terminal ballistic-elastic device. **a,** A general situation with various asymmetries. **b,** Abstraction in terms of quasi-equilibrium reservoirs and transmission functions (τ_{12} and τ_{21}). **c,** Incorporating an inelastic thermal collimator between reservoir and test section fundamentally changes the nature of the energy entering the test section, from quasi-equilibrium Bose-Einstein distributions to non-equilibrium distribution functions which depend non-linearly on both T_1 and T_2.

Aspect Ratio: $\alpha = H/D$
Porosity: $p = D^2/L^2$
Temperature Ratio: $\tau = T_{BBC}/T_{Col.}$
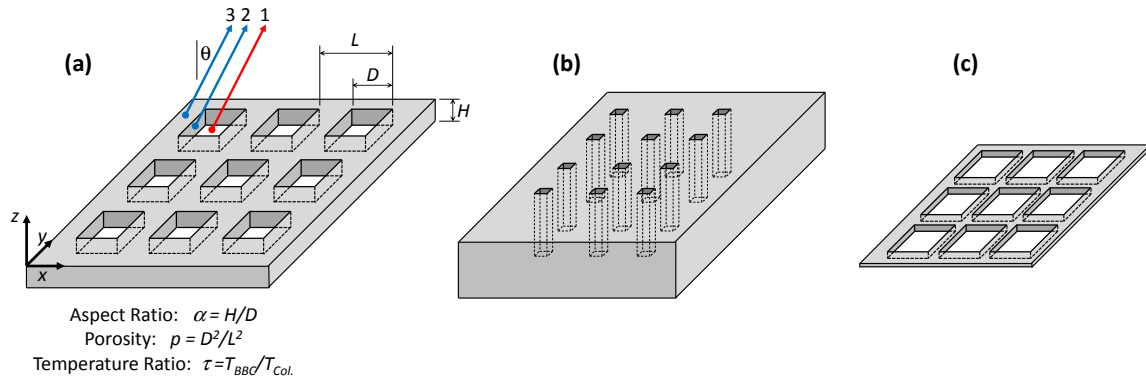
Supplementary Figure 6 | Analyzing the effect of the collimator aspect ratio. **a,** Schematic, showing the three types of surface that contribute to radiation in a given direction θ. The analysis uses square pores for simplicity. **b, c,** Limiting geometries for large and small aspect ratios, respectively.

6
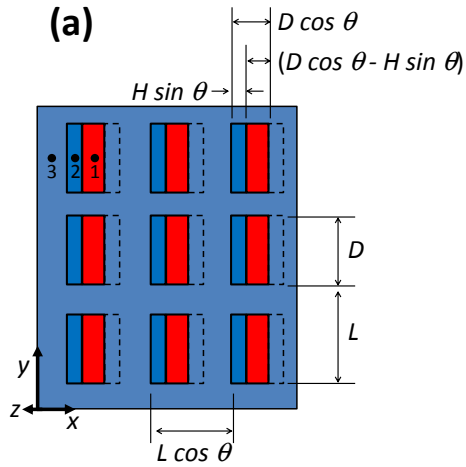
(a) View of collimator from along θ, exhibiting foreshortening.
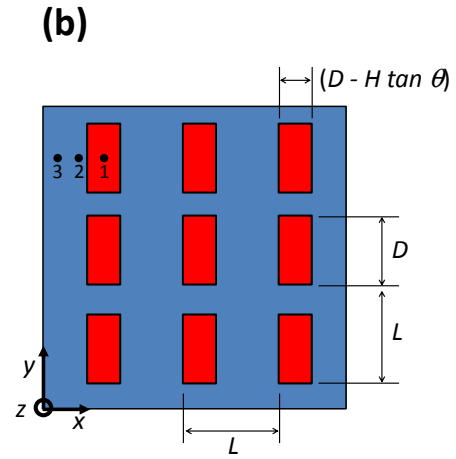
(b) View from along *z*, of a *flat* sheet which gives the same emission *along θ*.

Supplementary Figure 7 | Details of the trigonometric projection used to determine an equivalent flat sheet. **a**, View of the 3D collimator from Supplementary Fig. 6a along a particular direction θ. The square features in the *xy* plane are foreshortened into rectangles in this view. **b,** An equivalent 2D flat sheet in the xy plane, which when viewed along θ will give the same radiation emission as in **a**.
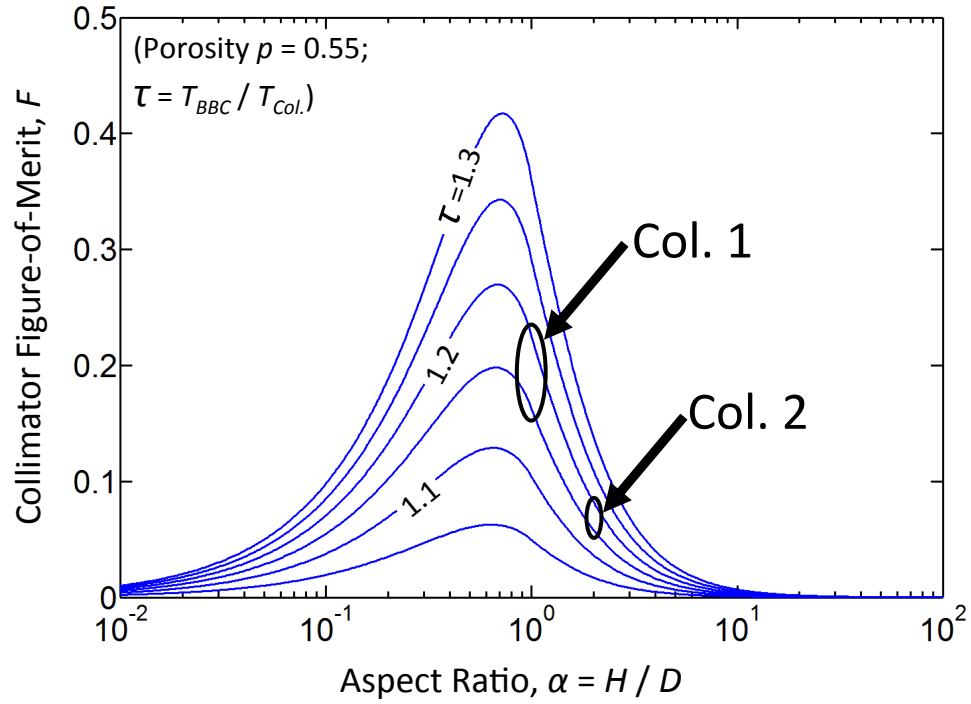
Supplementary Figure 8 | Results of the collimator calculation, with parameters chosen to approximate the actual experimental conditions (p=0.55, $\tau\approx$1.15 - 1.2, and α=1 and 2). This calculation shows that the optimal aspect ratio of the collimator pores is slightly below unity, and helps explain why the rectification performance of Collimator 2 (α=2) was significantly worse than that of Collimator 1 (α=1).
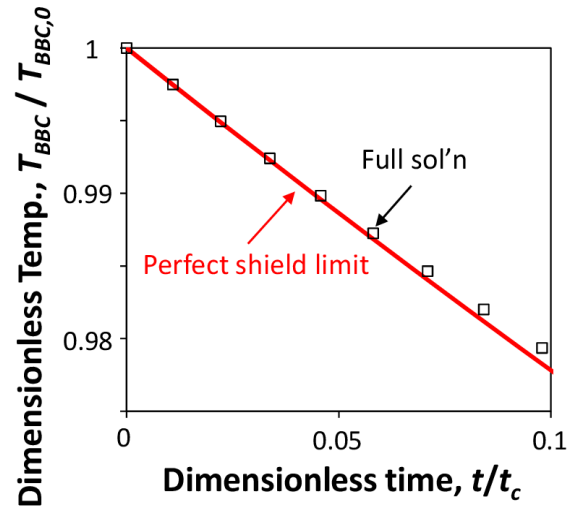
Supplementary Figure 9 | Comparing the solution from the perfect shield limit to the full solution of the lumped cooling model. Using realistic parameters, the difference between the perfect shield limit of Supplementary Eq. (15) and the full numerical solution of Supplementary Eq. (13) is estimated to be less than 0.1% over the typical experimental regime $t/t_c < 0.1$, where $t_c \sim 7$ hours (see text).
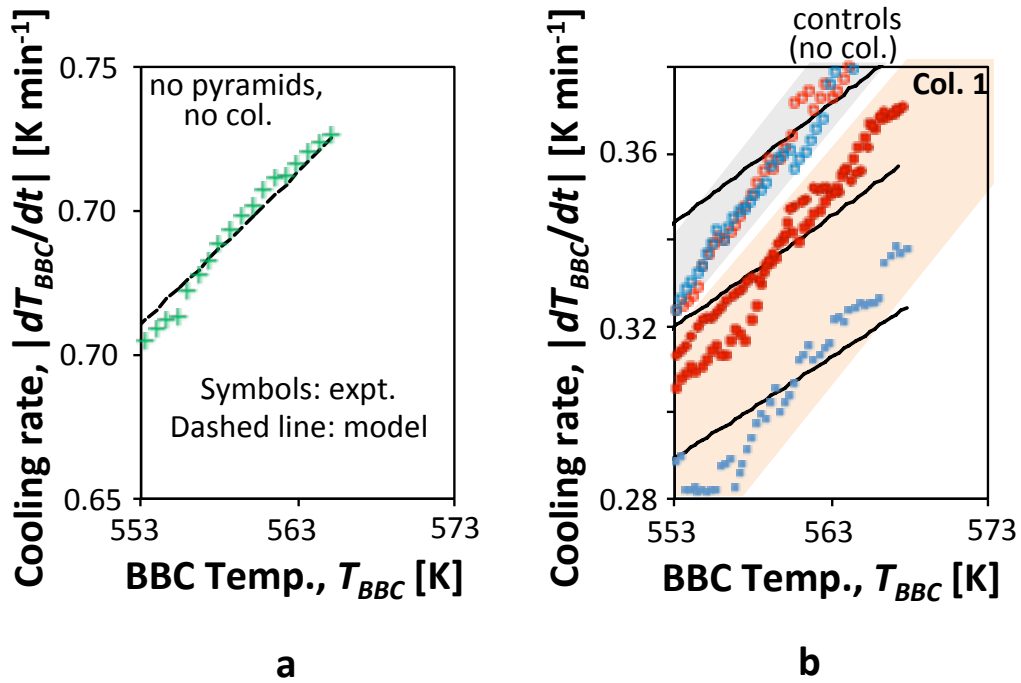
Supplementary Figure 10 | Comparing experimental results to the constant radiation resistor model. Each curve has one free parameter. **a**, For the simplest scenario of no collimator or pyramidal test section, the model agrees with the experiment to within 1.5%. **b**, For experiments involving the test section and collimator, this simple linear model explains the average magnitude of the experimental results. The slopes of **b** are in error but this may not be surprising considering the additional complexity and nonlinearity involved. For clarity we only fit three of the five cooling curves of Fig. 3b (see text).

(a) Top View

(b) Cross-section
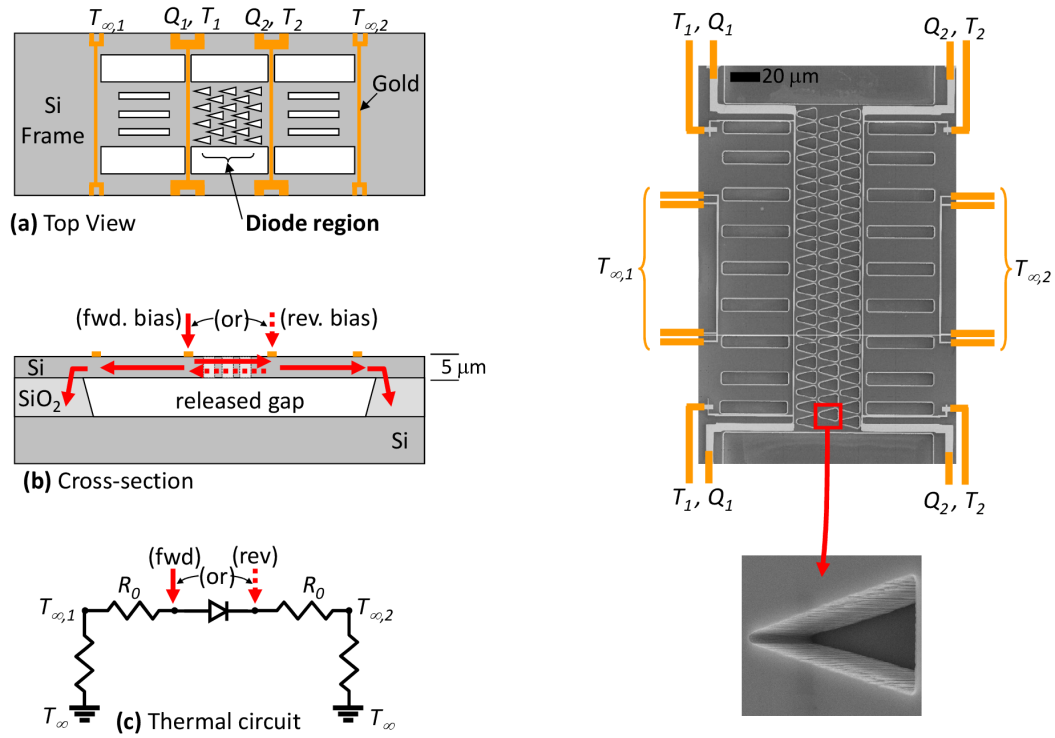
(c) Thermal circuit

Supplementary Figure 11 | An experiment to study thermal rectification of phonons by asymmetric microfabricated pores. Left: Concept and thermal circuit. Right: A fabricated structure. Since this structure lacks an inelastic thermal collimator, no rectification is expected.
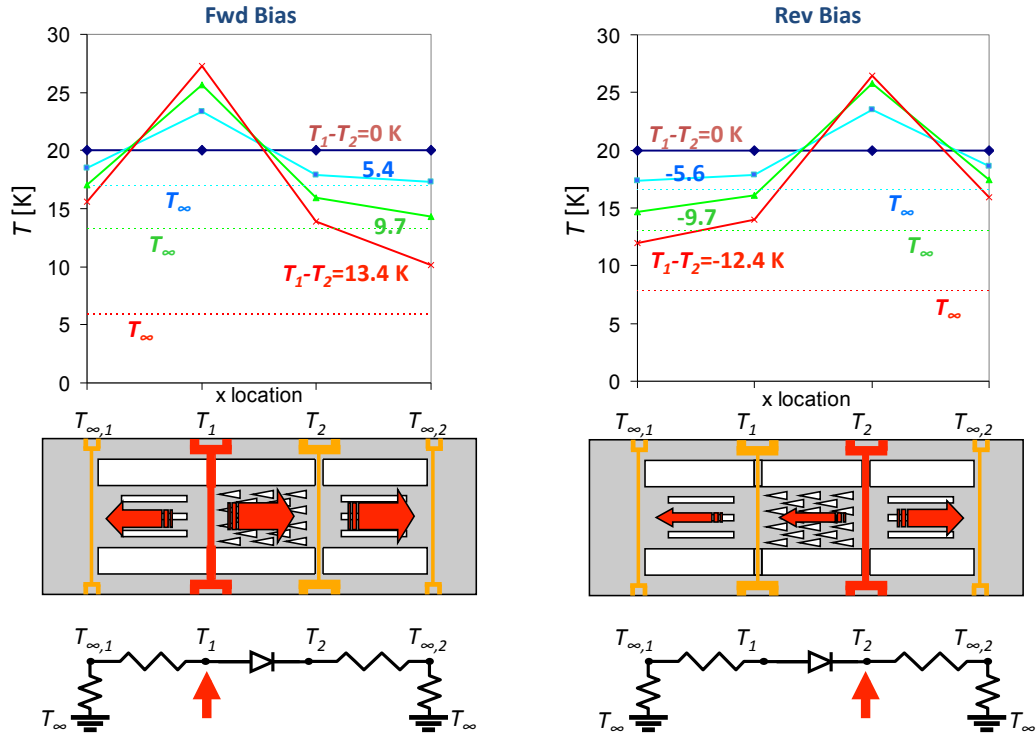
Supplementary Figure 12 | Attempted phonon thermal rectification: typical experimental data in forward and reverse bias (left and right columns, respectively). Top: Measurements. Bottom: Corresponding schematics. In each experiment the test section (diode region) is between the points labeled T_1 and T_2. The average temperature was fixed at 20 K, while 4 different thermal biases were applied: $\Delta T \approx \pm(0, 5.5, 9.7,$ and 13) K. Rectification corresponds to $(T_2 - T_{\infty,2})_{Fwd} > (T_1 - T_{\infty,1})_{Rev}$. Because the two plots are basically mirror images of each other, there is no clear rectification above the noise threshold. This null result is expected due to the fact that rectification is not possible without an inelastic thermal collimator.

Supplementary Note 1: Design of the blackbody cavity (BBC)

Although for simplicity the main text is written as if both reservoirs are perfectly black, the fundamental analysis of the ballistic thermal rectification mechanism applies just as well to reservoirs with arbitrary spectral, directional, emissivity functions $\varepsilon(\lambda,\theta,\varphi,x,y)$. Importantly, the analysis predicts that even for an arbitrary asymmetric test section and both reservoirs with their own arbitrary $\varepsilon(\lambda,\theta,\varphi,x,y)$, rectification cannot occur without the introduction of some explicit nonlinearity[1] (here, the inelastic thermal collimator). For simplicity in the discussion and interpretation of the experiments, we endeavored to use reservoirs that are approximately black, i.e. $\varepsilon \approx 1$ for all λ, θ, φ, x, and y across the aperture. Here we followed standard BBC designs to approach this ideal[2]. Graphite was chosen as the BBC material because of its relative high intrinsic emissivity ($\varepsilon = 0.80$ at room temperature, increasing with temperature in the experimental regime[3]), good high temperature stability, and machinability by the supplier (Poco Graphite). The total directional emissivity [$\varepsilon(\theta, \varphi)$] of our resulting BBC design is at least 0.91 from all (x,y) across the aperture[2].

One major design criteria for heat transfer is to ensure the large majority of the BBC's heater power transmits through the BBC aperture (and thus the test section) instead of being lost from the exterior of the BBC's side walls. This is difficult because the transmit-to-loss ratio scales with the area ratio of the aperture to the external BBC surfaces, and thus clashes with the design criteria for a high effective emissivity of the aperture[2]. In other words, a larger aperture increases the transmit-to-loss ratio, but decreases the effective emissivity of the aperture. To overcome this difficulty, a guarding + shielding concept (Supplementary Fig. 1a) is implemented. A guard heater (graphite) is designed to create a local surrounding temperature approximately equal (±1 K) to the temperature of the BBC, thus greatly reducing the radiation loss from the BBC. The BBC and guard each have two independent heater loops (Supplementary Fig. 1b), made by hand winding heater wires of nickel-chromium alloy (Omega Engineering, NIC80-010-062 and NI80-040; insulated with steatite "fish spine" beads, FS-200-14, $k \approx 5$ W/m-K), and anchored with cement (Resbond-920, $k \approx 2.2$ W/m-K) along 15% of their length. We press fit six K-type thermocouples into the graphite (Supplementary Fig. 1a): one at the center of each heater zone (Supplementary Fig. 1b) to provide feedback to the PWM controllers; plus one at the edge of each BBC zone to check the temperature uniformity of the BBC. The worst case non-uniformity is found to be 1.5 K from the center to the edge of the BBC side wall.

Five concentric radiation shields (Supplementary Fig. 1a; polished copper, $\varepsilon < 0.05$[4]) are placed between the guard heater and BBC (top, sides, and bottom), with another five radiation shields placed outside the pyramidal test section to further reduce the radiation loss. Five more concentric radiation shields are placed outside the guard heater (top, sides, and bottom) to further reduce the power requirements of the guard heater. With this design, at steady state the heat loss through the BBC side walls is estimated to be < 1% of the heating power $P_{BBC} = [I \cdot V]_{BBC}$. In this estimation, we exploited a standard radiation shield calculation[5,6] with the following conservative parameters: $T_{BBC} = 573$ K, $T_{BBC} - T_{guard} = 2$ K, $\varepsilon_{Cu} = 0.1$, and the realistic geometries from the actual concentric cylinders, including details such as the top caps with square openings. Because these experiments are always operated in high

vacuum, we observe that the copper surface remains bright and shiny even after many days of operation.

Finally, to minimize conductive losses we use four hollow ceramic pegs to support the BBC above the guard heater, and another four pegs to support the whole system above the vacuum chamber floor. Each peg has length 1.50", wall thickness 0.039", and outer diameter 0.156"; to accommodate the thermal expansion mismatch between graphite and copper the through-holes on the radiation shields have diameters 0.190". The resulting heat conduction through the ceramic pegs is estimated to be < 0.1% of the power transmitting through the test section.

Supplementary Note 2: Asymmetric transmission functions

The starting point of this ballistic thermal rectification mechanism is based on the intuition depicted in Fig. 1a of the main text: the ballistic trajectories directed towards the peaks of the pyramidal arrays (τ_{12}; here 1 denotes the test section terminal facing the peaks of the pyramids, and 2 denotes that facing the bases) have high transmission for normal incidence, while the ballistic trajectories incident on the bases of the pyramidal arrays (τ_{21}) have high transmission for oblique incidence.

One fundamental question may arise regarding this intuition: is it possible to achieve τ_{12} = 100% while τ_{21} = 0% for all incident positions and angles? The answer is no. A qualitative argument is based on time reversal symmetry: for each transmitted trial along one direction, there must exist a corresponding trial which follows exactly the same path but in the opposite direction. It is impossible to block one trial without blocking the other. This insight has been quantified using a Landauer-Büttiker approach[1,7]; see also Supplementary Note 4 below for a more extensive discussion.

In order to guide the design of the experimental test section, we simulated the scattering of photons by asymmetric pyramidal structures using a ray tracing scheme in a three dimensional domain[1,8]. Supplementary Fig. 2a shows the geometry used in the main work, which was crudely optimized using a phenomenological drifted Bose-Einstein model of the inelastic thermal collimator[1,8]. The chosen structure is a double layer of pyramidal arrays. Each layer is a "checkerboard" array, and the first layer is staggered with respect to the second layer. Each pyramid is treated as perfectly specular, and has an aspect ratio (AR) of 3:1 (height:base). The gap between the tips of the lower layer and the bases of the upper layer is equal to one-half of the base of a pyramid. To improve the computational efficiency, we define our ray-tracing simulation domain using a unit cell (indicated using black dashed lines) by considering the mirror symmetries of the staggered pyramidal arrays. For each polar angle ($\Delta\theta$ mesh of 1 deg.), the transmission coefficient is averaged over 9604 photon trials, in which the x-y position and azimuthal angle φ are randomized with uniform distribution using a Monte Carlo (MC) scheme. Supplementary Fig. 2b shows the results, with 95% confidence intervals in τ estimated as <1% for all θ. For transport towards the peaks (τ_{12}^{θ}, red line), photons of near-normal incidence ($\theta = 0^{\circ}$) are largely transmitted, while photons incident from oblique angles are largely reflected. For transport towards the

bases (τ_{21}^{θ}, blue line), on the other hand, photons from $\theta = 0°$ are entirely reflected, and photons incident from oblique angles have higher transmission.

The pyramidal test section is designed according to these simulation results. To qualitatively confirm the as-fabricated test section meets its core function of having very different angle-dependent transmission coefficients from its two ends, we imaged the test section from various angles using visible light and a consumer-grade digital camera. This is a conservative check, since IR has a longer wavelength than visible light, and thus for fixed surface roughness it will perceive the pyramids as being more specular. In addition, the intrinsic reflectivity of copper in the IR is also higher than in the visible[4]. As shown in Supplementary Fig. 3a, we first cover the backside of the test section with a black cloth, and place it in a large environment that is otherwise white. The front side of the test section is then imaged with a digital camera located around 25" away (corresponding to a small solid angle of 0.010 sr) with two different angles: normal ($\theta = 0°$) and oblique ($\theta = 45°$). The camera exposure time is the same for all four scenarios.

For the configuration with pyramid peaks pointing away from the black cloth (Supplementary Fig. 3a), the view from $\theta = 0°$ is almost totally black, indicating the large majority of photons incident from this direction are transmitted through to the black cloth. On the other hand, the image from $\theta = 45°$ shows much less black, indicating that most photons incident from $45°$ are reflected. The observations for the configuration with pyramid peaks pointing down towards the black cloth (Supplementary Fig. 3b) are opposite: the photographs are mostly shiny from $\theta = 0°$, indicating low transmission, and much more black from $\theta = 45°$ (higher transmission). The trends of this semi-quantitative experiment are consistent with the ray tracing results of Supplementary Fig. 2b and confirm that the transmission functions of the fabricated test section indeed have the required angular dependencies.

Supplementary Note 3: Nonlinearity of the thermal transport

The "nonlinearity" in this work refers to the bias dependence (ΔT) of the angular intensity weighting function, w. It is important not to confuse this with the nonlinear concept in optical media, which describes a material whose polarization responds nonlinearly to the electrical field, resulting in field-dependent optical properties such as the absorption coefficient. In this spirit, we can describe w using a *bias-dependent* directional emissivity, $\varepsilon(\theta, \Delta T)$, as follows.

We emphasize that a *static* angle-dependence in $\varepsilon(\theta)$, no matter how sharply peaked[9], cannot lead to thermal rectification. The key is to introduce some additional bias dependence as well. In our work this is realized through the inelastic thermal collimator.

We now use Supplementary Fig. 4 to present an intuitive explanation for this bias dependence, with a more complete analytical treatment given later in Supplementary Note 5. Supplementary Fig. 4 depicts the evolution of the distortions in the weighting function, $w(\theta)$, caused by increasing ΔT. For simplicity here we imagine the graphite of the collimator to be perfectly black; allowing for $\varepsilon_{graphite} < 1$

15

does not change the major trends. We fix T_{BBC} = 573 K for all three scenarios, but vary the temperature of the surroundings (T_∞), and thus the bias (ΔT). In response, the collimator temperature passively floats to some intermediate value, $T_\infty < T_{col.} < T_{BBC}$, where the exact value of $T_{col.}$ is unknown in practice and depends on T_{BBC} and T_∞ in a complicated fashion.

At zero bias (ΔT = 0 K) as depicted in Supplementary Fig. 4a, the whole system is in equilibrium and so the temperature of the graphite collimator ($T_{col.}$) is also at 573 K. Thus, the combined effect of BBC + collimator is to emit photons into the pyramid test section with an isotropic Lambertian distribution, characterized by a radiation temperature of 573 K at all angles.

For non-zero bias (Supplementary Fig. 4b&c) however, $T_{col.} < T_{BBC}$. Now, due to the open holes in the collimator, for angles close to $\theta \approx 0°$ many of the photons entering the pyramid test section were emitted from the BBC core at T_{BBC}. But photons at oblique angles are much more likely to have been emitted from the internal cylindrical surfaces of the collimator holes, with lower intensity since $T_{col} < T_{BBC}$. Thus, the photons have a distribution distorted away from Lambertian after passing through the collimator. The higher the bias, the more distorted the distribution, and thus the higher the expected rectification.

Supplementary Note 4: The distinction between an "inelastic thermal collimator" and a conventional optical collimator

A complete theoretical analysis of this thermal rectification mechanism is beyond the scope of the present work. Here we outline some key theoretical results to better clarify the meaning of "inelastic thermal collimator" and "nonlinearity" as used in this study. A more complete analysis is in preparation[10].

Supplementary Fig. 5a shows a generic ballistic thermal rectifier, with adiabatic side walls except for energy exchange between reservoirs 1 and 2. Many asymmetries are possible, including the device sidewall shape and internal structures which may act as filters, refractive index gradients, lenses, and mirrors. We specifically note that a *conventional* collimator as normally used in optics is made simply of mirrors and/or lenses, and so is subsumed in the above list.

The reservoir contacts in Supplementary Fig. 5 may be selective emitters with arbitrary spectral and directional emissivities $\varepsilon(x, y, \theta, \varphi, p, \omega)$[5,6], where ω is frequency and p polarization. This is equivalent to spectral and directional filtering of an ideal blackbody.

For a photon of wavevector **k** and polarization p leaving reservoir 1 and incident on the left contact at location $\mathbf{x}_1$, the transmissivity $\tau_{12}(\mathbf{x}_1, \mathbf{k}, p)$ is the probability of the photon entering the device and ultimately being absorbed in reservoir 2 (Supplementary Fig. 5b). Because all interactions within the test section are purely elastic (energy conserving), the only other possible fate of this photon is for it to be re-absorbed in reservoir 1. That is, $\tau_{11}(\mathbf{x}_1, \mathbf{k}, p) = 1 - \tau_{12}(\mathbf{x}_1, \mathbf{k}, p)$. We see that τ_{12} is purely a geometric and spectral property of the system, and is independent of the temperature of the device and contacts.

Wave effects are permitted, including coherent interference phenomena such as localization. This system satisfies the principle of microscopic reversibility and thus detailed balance[11].

We calculate the net thermal transport using a Landauer-Büttiker approach[12–14]. When the reservoirs are out of equilibrium, the net heat flow Q is the difference between the dynamic heat flows from left-to-right (Q_{12}) and right-to-left (Q_{21}), where

$$Q_{ij} = \tfrac{1}{8\pi^3}\sum_p \iint_{\mathbf{k}\,\mathbf{x}_i} \tau_{ij}\hbar\omega\, f_i\, \mathbf{v}\cdot\mathbf{n}_i\, d^2\mathbf{x}_i\, d^3\mathbf{k}\,. \tag{1}$$

Here $\mathbf{v}$ is the group velocity within the reservoir, $\mathbf{n}_i(\mathbf{x}_i)$ is the local unit normal of the contact surface (directed into the device), and f_i is the distribution function within reservoir i.

The standard boundary condition for a blackbody reservoir is Lambertian (or "cosine-law") emission, where the emitted radiation intensity is uniform in all directions[5,6] and characterized by Bose-Einstein statistics f_{BE} according to the reservoir temperature. It has been shown[1,7,10] that such quasi-equilibrium reservoirs cannot give thermal rectification for any conceivable combination of the energy-conserving elements depicted in Supplementary Fig. 5a and described above. To see this, for reservoirs at T_1 and T_2 the net heat transfer can be written

$$Q(T_1,T_2) = \int_\omega \left[f_{BE}(\omega,T_1)H_1(\omega) - f_{BE}(\omega,T_2)H_2(\omega)\right]d\omega\,, \tag{2}$$

where

$$H_1(\omega) = \tfrac{1}{8\pi^3}\sum_p \int_{\theta,\varphi,\mathbf{x}_1} \frac{\tau_{12}\hbar\omega\, \mathbf{v}\cdot\mathbf{n}_1\, d^2\mathbf{x}_1 |\mathbf{k}|^2 \sin\theta\, d\theta\, d\varphi}{\mathbf{v}\cdot\hat{\mathbf{k}}}\,, \tag{3}$$

and similarly for H_2 upon exchanging $1\leftrightarrow2$ and multiplying by -1. Here θ and ϕ give the direction of $\hat{\mathbf{k}}$ with respect to some reference[10]. Thus, H_1 and H_2 are spectral transfer functions, dictated by the system specifications through τ_{12} and τ_{21} [14,15].

At thermal equilibrium, the 2nd Law of Thermodynamics requires that $Q=0$ and $T_1=T_2=T$. Because this balance must hold for arbitrary T, it follows from Supplementary Eq. (2) that

$$H_1(\omega) = H_2(\omega) = H(\omega) \tag{4}$$

for all ω. Remarkably, regardless of the geometric and spectral asymmetries built into the device (which determine τ_{12} and τ_{21}), we find that $H_1(\omega)$ and $H_2(\omega)$ must always be equal. Thus, the detailed *geometric and spectral* quantities $\tau_{12}(\mathbf{x}_1,\theta,\phi,\omega,p)$ and $\tau_{21}(\mathbf{x}_2,\theta,\phi,\omega,p)$ are coupled by the integral *thermodynamic* constraint of Supplementary Eq. (2). Interestingly, this constraint is equivalent to the conservation of etendue in optical terminology[16], which also is essentially the reciprocity relation of view factor analysis[5,6] in radiation heat transfer.

Returning to a non-equilibrium condition, substituting Supplementary Eq. (4) into Supplementary Eq. (2) immediately shows that for quasi-equilibrium reservoirs we always have $Q(T_H,T_C) = -Q(T_C,T_H)$, where T_H and T_C are the hot and cold temperatures of interest. Thus, for any conceivable $H(\omega)$, the quasi-equilibrium reservoir approximation requires the net heat transfer to be antisymmetric upon exchanging T_1 and T_2. This is true regardless of the detailed internal structure of Supplementary Fig. 5a. This major constraint is a direct consequence of the 2nd Law of Thermodynamics, and can also be readily shown from reciprocity considerations[7].

Some kind of nonlinearity is needed to overcome this constraint. Accordingly, in the present work we introduce an "***inelastic thermal* collimator**." Abstractly, the function of the collimator at reservoir 1 is to modify the reservoir's emission so that it now depends on T_2 as well as T_1 (see Supplementary Fig. 5c). Put another way, instead of the *linear* reservoir boundary condition $f_1(\omega) = f_{BE}(\omega,T_1)$, the inelastic thermal collimator yields a *non-linear*, non-equilibrium boundary condition $f_1(\omega) = f_{NE,1}(\omega,T_1,T_2)$. Now Supplementary Eq. (2) is

$$Q_{Fwd} = \int_\omega \left[f_{NE,1}(\omega,T_H,T_C) - f_{NE,2}(\omega,T_C,T_H) \right] H(\omega) d\omega , \tag{5a}$$

$$Q_{Rev} = \int_\omega \left[f_{NE,1}(\omega,T_C,T_H) - f_{NE,2}(\omega,T_H,T_C) \right] H(\omega) d\omega . \tag{5b}$$

Now there is no reason to expect any special symmetry of $f_{NE,1}$ and $f_{NE,2}$, since they both interact with the test section which itself is asymmetric. Thus, this result shows how it is now mathematically possible to achieve rectification.

We give the name "inelastic thermal collimator" to this component because its most desirable feature is that at high bias its emission is strongly forward-peaked; this is loosely analogous to a conventional optical collimator which receives light from different angles and emits it with a tighter focus. However, from the discussion and equations above, it should be clear that the inelastic thermal collimator is quite different from a conventional optical collimator. Most crucially, the inelastic thermal collimator interacts with the photons inelastically: in an effective *inelastic thermal collimator*, a substantial fraction of the photons are absorbed and reemitted at a different energy, and their number is not conserved. On the other hand, a *conventional optical collimator* interacts with photons purely elastically (reflection and transmission, but no absorption or emission), their number is conserved, and its temperature never enters into the physical picture.

Supplementary Note 5: A simple model for the aspect-ratio optimization of the inelastic thermal collimator

An accurate model for the non-equilibrium collimator is desired but challenging, because the complicated 3D geometries of collimator and test section make it quite difficult to calculate the collimator temperature $T_{col.}$ (recall that $T_{col.}$ floats between T_{BBC} and T_∞, e.g. see Supplementary Fig. 4). Consider the schematic collimator depicted in Supplementary Fig. 6. For simplicity and to focus on the

main physics, we approximate the holes as squares rather than circles, and treat the collimator surfaces as black and diffuse. Referring back to Supplementary Fig. 4, the key to understanding the emitted radiation along given polar angle direction θ is that it is made up of three contributions. First is the direct emission from the BBC, representative of T_{BBC} and indicated by arrow #1 in Supplementary Fig. 6a. In addition, the collimator also contributes some emission characteristic of $T_{Col.}$, from both its internal pore walls (arrow #2) and its upper surface (arrow #3).

For an effective inelastic thermal collimator, the radiation at small θ should be dominated by T_{BBC}, while the radiation at large angles should be dominated by $T_{col.}$, as shown in Supplementary Fig. 4. In the limits of large and small aspect ratio ($\alpha \equiv H/D$), it becomes apparent by inspection that the collimator fails. For example, for high aspect ratio holes (Supplementary Fig. 6b), the BBC can contribute very little radiation, even for emission close to θ = 0°, and so the entire radiation field leaving the collimator corresponds only to T_{col}. Similarly, for large porosity and very small aspect ratio pores (Supplementary Fig. 6c), the radiation leaving the collimator is dominated by T_{BBC}. Therefore, the optimal aspect ratio must be somewhere in between 0 and ∞.

To develop a quantitative estimate from these physical insights, we used textbook radiation theory [5,6] to analyze the emitted radiative power from the generic structure shown in Supplementary Fig. 6a. (Because intensity is uniform in (θ,φ) for a black surface[5,6], the analysis is simplified by 2D projections to consider equivalent flat sheets, as indicated in Supplementary Fig. 7b.) We are concerned with the radiative power leaving the collimator and entering the test section, which is given by

$$Q = \int \iiint I \cos\theta \, dA \, \sin\theta \, d\theta \, d\varphi \,, \tag{6}$$

where here the intensity $I(x,y,\theta,\varphi) = \frac{1}{\pi}\sigma T^4$ for black diffuse surfaces, and σ is the Stefan-Boltzmann radiation constant. Since the θ dependence is critical, the quantity of most interest is

$$Q_\theta = 2\pi\sigma \iint \frac{1}{\pi} T^4 \cos\theta \sin\theta \, dA \,, \tag{7}$$

with units [W/rad]. This form assumes azimuthal symmetry, which greatly simplifies the analysis and is a reasonable first approximation for the square pores used below.

According to the crossing between the Fwd and Rev transmission curves as shown in Supplementary Fig. 2, we choose a threshold angle θ_c=45° to distinguish between photon trajectories that are predominately normal incidence into the test section, and those that are predominately oblique incidence. Therefore, a good collimator is one whose emission is dominated by T_{BBC} for $0 \leq \theta \leq 45°$ but dominated by $T_{col.}$ for $45 < \theta \leq 90°$. For fixed T_{BBC} and $T_{col.}$, we quantify this by introducing a collimator figure-of-merit,

$$F = \frac{Q_{0-45} - Q_{45-90}}{\frac{1}{2}(Q_{0-45} + Q_{45-90})} \,, \tag{8}$$

where the notation Q_{a-b} represents the total emission in the angular band $a° \leq \theta \leq b°$:

$$Q_{a-b} = \int_{a^\circ}^{b^\circ} Q_\theta \, d\theta \,. \tag{9}$$

Emission from the open area of the base of the pores occurs at T_{BBC} (ray #1), while rays #2 and #3 occur at T_{col}. To avoid tedious trigonometry we perform the detailed calculation only for the azimuthal angle aligned with the x axis. As polar angle θ increases, the view factor from the test section to the pore base is gradually occluded by the pore sidewalls, and beyond a critical shadowing angle $\theta_{sh} = \tan^{-1}(D/H)$ there is no contribution from T_{BBC} at all. See Supplementary Fig. 7a.

The results of this calculation are shown in Supplementary Fig. 8 for a porosity of p=0.55, corresponding to the collimators used in the experiments. The temperature ratio τ between BBC and collimator is unknown in the experiments, but was estimated to be in the range 1.15 - 1.2 based on a rough measurement with a temporary thermocouple. Supplementary Fig. 8 confirms that collimator performance goes to zero for both large and small α, as expected from the qualitative arguments given earlier. It also confirms that collimator performance should improve with thermal bias (parameterized here by τ), consistent with the measurements shown in Fig. 4 of the main text. Additional calculations (not shown) show that the optimal porosity is p=1, which in practice is limited by the mechanical integrity of the collimator.

Finally, we note that the optimum aspect ratio according to this calculation is slightly below unity. Since the collimators used in our experiments had aspect ratios of α=1 (Col. 1) and α=2 (Col. 2), this calculation helps explain why the rectification performance of Collimator 2 was inferior: its aspect ratio was too large for optimum, and thus performance was degraded (Compare filled and striped columns in the experiments of Fig. 3 of the main text).

Supplementary Note 6: Lumped cooling model

We explain the lumped cooling model used to develop Eqs. (2) and (3) of the main text. The lumped cooling problem is the thermal-domain analogy of discharging an electrical RC circuit. The Biot number during the cooling process is estimated to be < 0.01, making the lumped cooling model a good approximation[17]. The basic energy balance on the dashed control volume in Fig. 2b of the main text yields

$$C_{BBC} \frac{dT_{BBC}}{dt} = P_{BBC} + Q_{BBC-G} - Q_{diode}, \tag{10}$$

where C_{BBC} is the thermal capacitance of the BBC estimated from geometry and handbook data, and P_{BBC} = $[I \cdot V]_{BBC}$ is the electrical power delivered to the BBC. We follow a standard radiation resistor analysis[5,6], where the driving potential is σT^4 with σ as the Stefan-Boltzmann constant, and resistances carry units of m^{-2}. Thus,

$$Q_{BBC-G} = \left(\sigma T_G^4 - \sigma T_{BBC}^4\right)\big/ R_{BBC-G} \tag{11}$$

is the heat transfer from BBC to guard, and

$$Q_{diode} = \left(\sigma T_{BBC}^4 - \sigma T_\infty^4 \right) / R_{diode} \tag{12}$$

is the heat transfer through the test section.

The measurements reported in the main text are obtained as follows. After the whole system stabilizes with $T_{BBC} = T_G = 573$ K (typically 12 hours), we turn off the heaters of the BBC at time $t = 0$ ($P_{BBC} = 0$ for $t > 0$) while maintaining the guard at 573 K (Fig. 2c of the main text). Now the energy balance on the BBC simplifies to

$$C_{BBC} \frac{dT_{BBC}}{dt} = \frac{\sigma T_G^4 - \sigma T_{BBC}^4}{R_{BBC-G}} - \frac{\sigma T_{BBC}^4 - \sigma T_\infty^4}{R_{diode}} . \tag{13}$$

In the perfect-shield limit ($Q_{BBC-G}/Q_{diode} \ll 1$, checked below), this further reduces to

$$C_{BBC} \frac{dT_{BBC}}{dt} = - \frac{\sigma T_{BBC}^4 - \sigma T_\infty^4}{R_{diode}} . \tag{14}$$

After separating variables and integrating, we obtain a closed-form solution to Supplementary Eq. (14), albeit for $t(T_{BBC})$:

$$t = \frac{R_{diode} C_{BBC}}{4\sigma T_\infty^3} \left[f\left(T_{BBC}(t) \right) - f\left(T_{BBC,0} \right) \right], \tag{15}$$

where $f(x) = \ln\left(\frac{x + T_\infty}{x - T_\infty} \right) + 2\tan^{-1}\left(\frac{x}{T_\infty} \right)$.

We first compare this perfect shield limit [Supplementary Eq. (15)] to the full numerical solution of Supplementary Eq. (13). In this calculation we use the following realistic parameters: $C_{BBC} = 1700$ J K^{-1}, $R_{BBC-G} = 600$ m^{-2}, and $R_{diode} = 640$ m^{-2}. Here C_{BBC} is estimated based the BBC's geometry and specific heat capacity[4] averaged over the experimental regime, R_{BBC-G} is extracted from full-time cooling curves beyond the perfect shield limit, and R_{diode} is averaged over the experimentally extracted Fwd and Rev resistances. In Supplementary Fig. 9, we plot the dimensionless temperature, $\hat{T}_{BBC} = T_{BBC}/T_{BBC,0}$, as a function of a dimensionless time, $\hat{t} = t/t_c$, where $t_c = C_{BBC} R_{diode}/\left(4\sigma T_{BBC,0}^3 \right)$ is estimated to be ~7 hours. Within the time regime of the real experiment ($t/t_c < 0.1$), the difference between the two solutions is less than 0.1%, corresponding to a maximum error of 0.55 K for 553 K < T_{BBC} < 573 K. This verifies that the perfect shield limit is appropriate for the experimental regime presented in the main text.

We next compare the cooling rate, $|dT_{BBC}/dt|$, predicted by this perfect shield limit to experiments. We treat R_{diode} as the only free parameter, and fit the experimental cooling curves to Supplementary Eq. (14). As shown in Supplementary Fig. 10a for the simplest scenario of no test section or collimator, the

model fit (dashed lines) agrees with the experimental cooling rate (points) with maximum error of 1.5% from 553 K to 569 K. We consider this very good agreement. In addition, from the fitting result, R_{diode} = 266 m^{-2}, and based on the aperture area of (2.50″)^2 and standard radiation analysis[5,6], we estimate the total hemispherical emissivity of the aperture to be 0.93, which is consistent with the BBC design value (>0.91) described above in SI Section 1.

Supplementary Fig. 10b shows a similar comparison of this model with the measurements from Fig. 3b of the main text. For clarity, instead of fitting all five of the cooling curves in Fig. 3b, we only performed three fits: the reverse biased experiment, one of the two forward biased experiments, and likewise one of the two control experiments (no collimator). The fits again capture the leading order behavior $|dT_{BBC}/dt|$, but now deviate from the experiments in the higher order behavior $d(|dT/dt|) / dT$. Such deviations may not be surprising considering the additional complexity and nonlinearity introduced by the collimator and test section. We emphasize that in Fig. 3c of the main text the diode power is calculated using Eq. (2) which directly averages the experimental cooling rate in Fig. 3b from 569 K to 553 K, and does not invoke Supplementary Eq. (5). Thus the fact that Supplementary Eq. (5) deviates from the experiment in Supplementary Fig. 10b has no effect on the results in Fig. 3c.

Supplementary Note 7: Further verification of the need for an inelastic thermal collimator: An experiment on *phonons* in an etched silicon on insulator (SOI) wafer

The success of the *photon* thermal diode reported in the main text builds on lessons learned from an earlier study of ballistic *phonons* in etched SOI. This previous experiment lacked an effective inelastic thermal collimator and thus is expected to be unable to provide rectification. Here we briefly summarize this experiment and its main result.

We attempted several variations of the basic concept illustrated in Supplementary Fig. 11. The central test section (between T_1 and T_2 in the figure) contains a ballistic thermal diode made by etching asymmetric triangular pores in the device layer of an SOI wafer. The central test section was then undercut by a selective wet etch to release it from the substrate, for thermal isolation. The experiments were conducted in high vacuum to eliminate convection, and radiation losses were also negligible. Temperatures as low as 10 K were used to maximize the mean free paths (MFPs) of the phonons in Si and ensure ballistic transport, and in an attempt to achieve long phonon wavelengths for specular reflections from the etched pores . Gold lines were used as heaters and resistance thermometers. All samples were patterned using e-beam lithography.

Typical measurement results are shown in Supplementary Fig. 12. The plots show measured temperature at the four positions indicated from left to right as $T_{\infty,1}$, T_1, T_2, and $T_{\infty,2}$. The thermal diode is in the central section between T_1 and T_2. The etched slots between $T_{\infty,1}$ and T_1, and between T_2 and $T_{\infty,2}$, are as symmetric as possible and used to increase the thermal resistance R_0 to be comparable to the expected R_{diode}. In each experiment in this example, the average temperature $\frac{1}{2}(T_1+T_2)$ was held constant at 20 K, while several thermal biases (T_1-T_2) were applied. This required simultaneous tuning of

two independent inputs: the background temperature of the cryostat's cold finger, T_∞ (which is different from $T_{\infty,1}$ and $T_{\infty,2}$), and the Joule heating at the hot-side of the device (Q_1 in forward bias, and Q_2 in reverse bias). We used an iterative secant method to optimize both input parameters simultaneously during the experiment.

The raw data in Supplementary Fig. 12 can be understood by considering the different heat flows through the test section in forward and reverse bias. As indicated in the schematics, to maintain the same magnitude of $|\Delta T|=|T_1\text{-}T_2|$, more heat should flow through the central diode section in forward bias than in reverse bias. In forward bias, this heat must then flow through the neighboring region from the location T_2 to the location $T_{\infty,2}$. In reverse bias, on the other hand, the heat flow exiting the diode section must then flow from $T_1 \rightarrow T_{\infty,1}$. Therefore, when holding $|T_1\text{-}T_2|$ constant but reversing thermal polarity (as in the experiments of Supplementary Fig. 12), the signature of thermal rectification is ($T_2\text{-}T_{\infty,2}$)$_{\text{Fwd}}$ > ($T_1\text{-}T_{\infty,1}$)$_{\text{Rev}}$. Inspection of the measurements in Supplementary Fig. 12 indicate that no such rectification was evident, because for any given ΔT the measured ($T_2\text{-}T_{\infty,2}$)$_{\text{Fwd}}$ ≈ ($T_1\text{-}T_{\infty,1}$)$_{\text{Rev}}$ to within experimental uncertainty. Thus we conclude that the experiment depicted in Supplementary Fig. 12 again confirms one of the key conclusions of the main text: ballistic thermal rectification is not possible through asymmetry alone.

Several other configurations were tried with different temperature ranges, structures, and configurations, including an "H-bridge" concept similar in spirit to what was used in the electrical analogue[18]. In all cases no rectification was detectable, consistent with expectations since there was no inelastic thermal collimator.

In light of the understanding developed in the main text, we identify two key issues which would need to be addressed to observe significant ballistic thermal rectification in a phonon system such as Supplementary Fig. 11. First is the fact that calculations predict stronger rectification for specular rather than diffuse surfaces[1,8]. The structures of Supplementary Fig. 11 were prepared by reactive ion etching (RIE) and exhibit roughness which may not be negligible compared to the characteristic phonon wavelengths even at these low temperatures[19]. Smoother surfaces might be achievable by using focused ion beam (FIB) milling rather than RIE, reflowing Si using a high-temperature hydrogen anneal[20], or exploiting crystallographic anisotropy such the well-known 111 stop planes of KOH-etched Si.

The second issue is more fundamental: the need for effective thermal collimation. The experiments of Supplementary Fig. 12 were performed at low temperatures to ensure ballistic phonon transport and specular reflections, but this also quenches the inelastic (umklapp) phonon scattering and thus there is no nonlinearity analogous to the mechanism of Supplementary Fig. 4. We emphasize that strategies based on simply etching slots into the SOI film cannot function as an inelastic thermal collimator for phonons, because phonon-surface scattering is elastic and thus linear. In contrast, the inelastic photon thermal collimator of the main text involves highly inelastic interactions between the photons and the graphite, which is one of the main advantages of the photon approach for this first demonstration.

We note that measurements on a related etched silicon membrane configuration have recently been reported by Schmotz et al. [21]. That study used a laser as a Gaussian heat source and an optical

method for temperature mapping, and inferred thermal rectification from the shapes of the temperature fields away from the array of etched pores. Significant rectification was reported for a sample base temperature of 150 K, while no effect was noted at 300 K, attributed to the phonon MFPs becoming too short at room temperature. That work was discussed in terms of a Lambertian heat source, without any explicit nonlinearity. However, based on current understanding of Si MFPs at 150 K[19,22] a significant fraction would have experienced umklapp scattering at least once between the laser source and pore array; and this inelastic scattering is expected[1] to behave functionally very much like the nonlinear thermal collimator idea of the present work.

Supplementary **References**

1. Miller, J., Jang, W. & Dames, C. Thermal rectification by ballistic phonons in asymmetric nanostructures (HT2009-88488). *2009 ASME Summer Heat Transf. Conf.* (San Francisco, 2009).

2. Bedford, R. E. *Calculation of Effective Emissivities of Cavity Sources of Thermal Radiation*. *Theory Pract. Radiat. Thermom.* (1988).

3. Neuer, G. Emissivity measurements on graphite and composite materials in the visible and infrared spectral range. *Quant. InfraRed Thermogr.* **27,** 359–364 (1992).

4. Touloukian, Y. S. *Thermophysical Properties of Matter*. (IFI/Plenum, 1970-1979).

5. Siegel, R. & Howell, J. R. *Thermal Radiation Heat Transfer*. (Taylor & Francis, 1992).

6. Modest, M. F. *Radiative Heat Transfer*. (McGraw-Hill, 1993).

7. Maznev, A. A., Every, A. G. & Wright, O. B. Reciprocity in reflection and transmission: What is a "phonon diode"? *Wave Motion* **50,** 776–784 (2013).

8. Miller, J. & Dames, C. Thermal rectificaiton by ballistic phonons in asymmetric nanostructures. *Mech. Eng.* **Master,** (2009).

9. Rousseau, E. *et al.* Radiative heat transfer at the nanoscale. *Nat Phot.* **3,** 514–517 (2009).

10. Dames, C. & Miller, J. Ballistic rectification in the thermal domain: Basic mechanism and thermodynamic constraints. *Prep.*

11. Reif, F. *Fundamentals of Statistical and Thermal Physics*. (McGraw-Hill, 1965).

12. Imry, Y. & Landauer, R. Conductance viewed as transmission. *Rev. Mod. Phys.* **71,** S306–S312 (1999).

13. Rego, L. & Kirczenow, G. Quantized Thermal Conductance of Dielectric Quantum Wires. *Phys. Rev. Lett.* **81,** 232–235 (1998).

14. Mingo, N. & Broido, D. Carbon Nanotube Ballistic Thermal Conductance and Its Limits. *Phys. Rev. Lett.* **95,** 096105 (2005).

15. Segal, D. & Nitzan, A. Spin-Boson Thermal Rectifier. *Phys. Rev. Lett.* **94,** 34301 (2005).

16. Chaves, J. *Introduction to Nonimaging Optics*. (CRC Press, 2008).

17. Lienhard, J. H. & Lienhard, J. H. *A Heat Transfer Textbook*. 3rd edn., Problem 5.6 on pg.253 (Phlogiston Press, 2003).

18. Song, A. M. *et al.* Nonlinear Electron Transport in an Asymmetric Microjunction: A Ballistic Rectifier. *Phys. Rev. Lett.* **80,** 3831–3834 (1998).

19. Dames, C. & Chen, G. *Thermal Conductivity of Nanostructured Thermoelectric Materials*. *Thermoelectrics Handbook: Macro to Nano,* Chapter 42, CRC Press, ed. D. Rowe, 2005.

20. Thareja, Kant, Howe & Nishi. Structural Transformation of Silicon due to Hydrogen Ambient during Germanium Epitaxy on Silicon Nano-pillars. *Mat. Res. Soc. Spring Meet.* (2009).

21. Schmotz, M., Maier, J., Scheer, E. & Leiderer, P. A thermal diode using phonon rectification. *New J. Phys.* **13,** 113027 (2011).

22. Minnich, a. J. *et al.* Thermal Conductivity Spectroscopy Technique to Measure Phonon Mean Free Paths. *Phys. Rev. Lett.* **107,** 095901 (2011).